

Links between soil properties and steady-state solute transport through cultivated topsoil at the field scale

J. K. Koestel,¹ T. Norgaard,² N. M. Luong,² A. L. Vendelboe,² P. Moldrup,³
N. J. Jarvis,¹ M. Lamandé,² B. V. Iversen,² and L. Wollesen de Jonge²

Received 6 April 2012; revised 12 December 2012; accepted 21 December 2012.

[1] It is known that solute transport through soil is heterogeneous at all spatial scales. However, little data are available to allow quantification of these heterogeneities at the field scale or larger. In this study, we investigated the spatial patterns of soil properties, hydrologic state variables, and tracer breakthrough curves (BTCs) at the field scale for the inert solute transport under a steady-state irrigation rate which produced near-saturated conditions. Sixty-five undisturbed soil columns approximately 20 cm in height and diameter were sampled from the loamy topsoil of an agricultural field site in Silstrup (Denmark) at a sampling distance of approximately 15 m (with a few exceptions), covering an area of approximately 1 ha (60 m × 165 m). For 64 of the 65 investigated soil columns, we observed BTC shapes indicating a strong preferential transport. The strength of preferential transport was positively correlated with the bulk density and the degree of water saturation. The latter suggests that preferential macropore transport was the dominating transport process. Increased bulk densities were presumably related with a decrease in near-saturated hydraulic conductivities and as a consequence to larger water saturation and the activation of larger macropores. Our study provides further evidence that it should be possible to estimate solute transport properties from soil properties such as soil texture or bulk density. We also demonstrated that estimation approaches established for the column scale have to be upscaled when applied to the field scale or larger.

Citation: Koestel, J. K., T. Norgaard, N. M. Luong, A. L. Vendelboe, P. Moldrup, N. J. Jarvis, M. Lamandé, B. V. Iversen, and L. Wollesen de Jonge (2013), Links between soil properties and steady-state solute transport through cultivated topsoil at the field scale, *Water Resour. Res.*, 49, doi:10.1002/wrcr.20079.

1. Introduction

[2] Downward solute transport through soil is generally heterogeneous. It mostly takes place along preferential flow paths instead of homogeneously distributed through the whole soil pore space. Ever-increasing evidence has accumulated in recent decades that this is true at all spatial scales from the pore scale [e.g., *Carminati et al.*, 2008], over the Darcy or column scale [e.g., *Bloem et al.*, 2009; *Kasteel et al.*, 2005; *Schotanus et al.*, 2012], the plot scale [e.g., *Bouma and Dekker*, 1978; *Flury et al.*, 1994], and the field scale [e.g., *Bronswijk et al.*, 1995; *Butters et al.*, 1989; *Wild and Babiker*, 1976] up to the regional scale [e.g., *Kurunc et al.*, 2011; *Shaffer et al.*, 1995; *Iversen et al.*, 2011] and larger. It is crucial to take the spatial heterogeneity at all scales into account for obtaining quantitative

predictions of water flow and solute transport through soils, which are predominantly needed at the field scale or larger, namely, for managing environmental and agricultural resources. However, the direct measurement of soil solute transport properties is time consuming and cumbersome. Due to time and budget limitations they are almost exclusively restricted to small scales (Darcy scale and smaller). It is not possible to map solute transport properties at larger scales (regional scale and larger) by direct measurements.

[3] The heterogeneities in solute transport fronts or plumes are subject to the soils' pore structure, namely, the abundance, distribution, and connectivity of pores of different sizes [e.g., *Vogel*, 2000]. Meanwhile, it is possible to create detailed 3-D images pore spaces of undisturbed soil by means of X-ray tomography, providing resolutions in the micrometer scale [e.g., *Schlueter et al.*, 2011; *Wang et al.*, 2012]. With the help of X-ray tomography and similar noninvasive methods as neutron beam scattering [e.g., *Carminati et al.*, 2008] or positron emission tomography [e.g., *Boutchko et al.*, 2012], it is to expect that relationships between the soil pore-network geometry and the water flow and solute transport will be quantifiable within the near future. However, high-resolution imaging methods like X-ray tomography are to our knowledge restricted to sample sizes of a few decimeters and are presently not applicable in the field. It is therefore neither possible to deduce solute transport properties from detailed

¹Department of Soil and Environment, Swedish University of Agricultural Sciences (SLU), Uppsala, Sweden.

²Department of Agroecology, Aarhus University, Tjele, Denmark.

³Department of Biotechnology, Chemistry and Environmental Engineering, Aalborg University, Aalborg, Denmark.

Corresponding author: J. K. Koestel, Department of Soil and Environment, Swedish University of Agricultural Sciences (SLU), PO Box 7014, 750 07 Uppsala, Sweden. (john.koestel@slu.se)

pore-network images at large scales. Alternative methods are needed to infer to them.

[4] A way out may be offered by using proxy variables like soil texture, bulk density, or land use to estimate soil solute transport properties. The main assumption of this approach is that specific soil pore structures, and therefore also solute transport properties, develop not at random but are conditional to soil properties, land use, climatic conditions, etc., in other words the proxy variables stated above. Similar approaches have been referred to as pedotransfer functions since the late 1980s [Bouma, 1989; Wösten et al., 2001]. They have been widely applied with reasonable success for estimating bulk densities [e.g., Rawls, 1983; Tranter et al., 2007] or soil hydraulic properties [e.g., Schaap et al., 1998; Vereecken et al., 1989].

[5] The potential of pedotransfer functions for soil solute transport properties have been much less researched. This is not surprising since solute transport depends on the hydraulic conductivity which proved to be difficult to estimate from proxy variables [Vereecken et al., 2010]. The corresponding studies available in peer-reviewed literature therefore focus on relatively simple experimental conditions. These are predominantly experiments on small soil columns (Darcy scale) with an inert tracer and steady-state hydraulic initial and boundary conditions. Table 1 contains a nonexhaustive list of respective publications. It can be seen that foremost the clay content was found to be related to solute transport properties. In addition, soil aggregate or macrostructure [Vervoort et al., 1999; Shaw et al., 2000; Vanderborght et al., 2001], flow rate [Vanderborght et al., 2001; Koestel et al., 2012], and scale of experiment [Vanderborght and Vereecken, 2007; Koestel et al., 2012] were always found to be important when investigated. Besides soil bulk density, organic carbon content and soil texture in general were reported to be important (Table 1), whereas it is to note that the hydropedological proxies used by Jarvis et al. [2009, 2012] include all the three. For two of the latter three soil properties, contrasting results have been published stating that bulk density and organic carbon content appeared to rather have a subordinate influence on solute transport [Koestel et al., 2012].

[6] It is reasonable for establishing relationships between soil properties and solute transport properties to focus on small scales since the small-scale relationships are very likely fundamental to corresponding relationships at larger scales [Vogel and Roth, 2003]. It must however not be forgotten that properties that are valid on small scales need to be scaled up if they are to be generalized for larger scales [e.g., Kolenbrander, 1970; Mallants et al., 1996]. Therefore, studies relating local solute transport properties to larger areas are likewise important. However, such studies are very scarce. We are only aware of two that investigate flux concentrations. One of them was undertaken by Lenartz et al. [1997]. They conducted bromide leaching experiments under steady-state irrigation rates of approximately 0.033 cm h^{-1} on the undisturbed soil columns collected from two fields near Kiel (Germany) from a $15 \text{ m} \times 15 \text{ m}$ grid ($N_1=24$ and $N_2=36$) with the average clay contents of 10%. They found that 25% of all columns exhibited preferential flow taking the so-called “mobility index” with values smaller than 0.35 as an indicator. The mobility index MI was obtained by dividing the piston-

flow velocity by the velocity obtained from fitting the convection-dispersion equation (CDE) [Glueckauf et al., 1949; Nielsen and Biggar, 1962] to breakthrough curves (BTCs). The spatial distribution of MI over each of the fields was not random, and regions with preferential flow were clustered. The spatial correlation length appeared to be less than the sampling distance of 15 m. The histogram of MI was for both investigated field sites’ bimodal with one peak around 0.6 (denoted as nonpreferential flow) and another peak around 0.15 (denoted as preferential flow); the distribution of the dispersivity was highly right-skewed with the mean values of 2.67 and 1.05 cm for the two investigated fields, respectively, and coefficients of variation of approximately 100% for both fields.

[7] Another similar experiment was published by de Jonge et al. [2004] and Poulsen et al. [2006]. They investigated 42 undisturbed soil columns taken from a field in Røgen (Denmark) with an average clay content of 13.4% with a sampling distance of 5 m. Bromide was applied under steady-state irrigation of 1 cm h^{-1} . Poulsen et al. [2006] did not calculate the mobility index MI. However, they fitted the mobile-immobile model [Coats and Smith, 1964; van Genuchten and Wierenga, 1976] which provides a similar parameter, namely, the ratio between the mobile and the total water content which is often denoted as β . By multiplying β with $q q^{-1}$ where q (cm h^{-1}) is the water flow rate, it can be seen that β bears formal similarity to MI. Poulsen et al. [2006] found that the bromide transport velocity (derived from fitting the mobile-immobile transport model to the BTCs) as well as β were proportional to the clay content and the bulk density which were also mutually correlated. In addition, de Jonge et al. [2004] inferred from colloid transport properties that preferential macropore transport was only dominant in soil samples with clay contents larger than 13%.

[8] In this paper, we present data on the spatial distribution of local soil solute transport properties over an approximately 1 ha large field site, which will contribute toward the long-term goal of establishing pedotransfer functions for the solute transport properties of soil. Nonparametric measures describing the shape of tracer BTCs under constant rate irrigation were contrasted and compared with soil texture, organic carbon content, and bulk density. Besides spatial correlations, we also investigated the upscaled solute transport properties of the entire field.

2. Materials and Methods

2.1. Site and Soil Sampling

[9] Our experiments were carried out on soil sampled from a field site in Silstrup, northern Denmark ($56^\circ 55' 56.16''\text{N}$, $8^\circ 38' 43.91''\text{E}$). Two soil profiles have been described at this site, one of which was classified as an Alfic Argiudoll and the other as a Typic Hapludoll, according to the U.S. Department of Agriculture (USDA) soil classification system [Lindhardt et al., 2001; Kjær et al., 2007]. The soil texture varies between the silty loam and the loam (USDA texture classification). Below the plowed topsoil, the upper meter of the subsoil is heavily fractured and bioturbated and contains 100–1000 biopores m^{-2} . The field had been plowed in November 2008 to a depth of 23 cm and harrowed twice to a depth of 5 cm in

Table 1. A Nonexhaustive Overview for Literature Reporting Correlations of Soil Properties, Site Factors, and Experimental Conditions With Solute Transport Properties

Publication	Type of Samples	Number of Samples	Transport Distance (cm)	Lateral Scale (cm)	Investigated Soils	Most Prominent Observed Relationship
<i>Addiscott and Bailey</i> [1990]	Non-area covering	> 13	Not specified	Not specified	Diverse, containing between 5% and 56% clay	Permeability with clay content
<i>Quisenberry et al.</i> [1993]	Metastudy (from four publications)	11	≤30	Not specified	Diverse, containing between 1% and 21% clay	Displacement of antecedent moisture with clay content
<i>Smith et al.</i> [1995]	Non-area covering	48	7.6	8.2	Pachic Argiustolls ^a (arable), average clay content 26%	Bromide leaching with bulk density
<i>Lemartz et al.</i> [1997]	Area covering	24 and 36	10	5.7	Mollic Cambisol ^b (forest)+Dystric Gleysol ^b (arable); both soils contained between 5% and 15% clay	Fraction of mobile water with texture and organic carbon content
<i>Vervoort et al.</i> [1999]	Non-area covering	11	30	15	Typic Kandiuults, ^a containing between 4% and 51% clay	Preferential transport with soil macrostructure
<i>Shaw et al.</i> [2000]	Non-area covering	34	19.9	15	Grossarenic and Typic Kandiuults, ^a containing between 3% and 28% clay	Dispersion coefficient with clay content and soil aggregate size
<i>Goncalves et al.</i> [2001]	Non-area covering	24	15–20	34.1–42.5	Dystric Fluvisol, ^b Calcic Vertisol, ^b Calcic Cambisol, ^b Vertic Luvisol, ^b containing between 8% and 56% clay	Dispersion with organic matter and Mualem-van Genuchten parameters
<i>Vanderborght et al.</i> [2001]	Non-area covering		33–100	30–800	Gleyic-Plaggic Anthrosol, ^b Haplic Podzol, ^b Lamellic Arenosol, ^b Luvisc Arenosol, ^b Eutric Regosol, Eutric Luvisol, ^b Stagnic Albeluvisol, ^b containing between 1% and 25% clay	Increasing dispersivity with flow rate; mixing regime with soil macrostructure
<i>de Jonge et al.</i> [2004]/ <i>Poulsen et al.</i> [2006]	Area covering	42	20	20	Typic Haplodal ^a (arable); average clay content 13.4%	Fraction of mobile water with texture and bulk density
<i>Vanderborght and Vereecken</i> [2007]	Metastudy (from 57 publications)	635 ^c	5–532	Not specified	Diverse, clay content not specified	Dispersivity with scale of experiment
<i>Bedmar et al.</i> [2008]	Non-area covering	112	15	8	Typic Argiudolls, ^a containing between 17% and 31% clay	Dispersivity with clay content
<i>Jarvis et al.</i> [2009]	Metastudy (from 13 publications)	52 ^d	13–38	8–24	Diverse, clay content between 2.7% and 56%	Peak-arrival time with hydropedological proxies
<i>Jarvis et al.</i> [2012]	Metastudy (from 29 publications)	209 ^e	8–40	4–46	Diverse, clay content between 2.7% and 60%	Relative 5%-arrival time with hydropedological proxies
<i>Koestel et al.</i> [2012]	Metastudy (from 76 publications)	733 ^f	5–150	2.5–124	Diverse, clay content between 0% and 70%	Relative 5%-arrival time with clay content and water flux

^aUSDA classification.

^bWorld Reference Base for Soil Resources (WRB) classification.

^cApproximately 110 samples were also included in *Koestel et al.* [2012].

^dContains three samples from *Shaw et al.* [2000] and six samples from *Bedmar et al.* [2008].

^eContains all samples from *Jarvis et al.* [2009].

^fContains all samples from *Jarvis et al.* [2012], approximately 110 samples from *Vanderborght and Vereecken* [2007], and samples from *Goncalves et al.* [2001], *Poulsen et al.* [2006], and *Vervoort et al.* [1999].

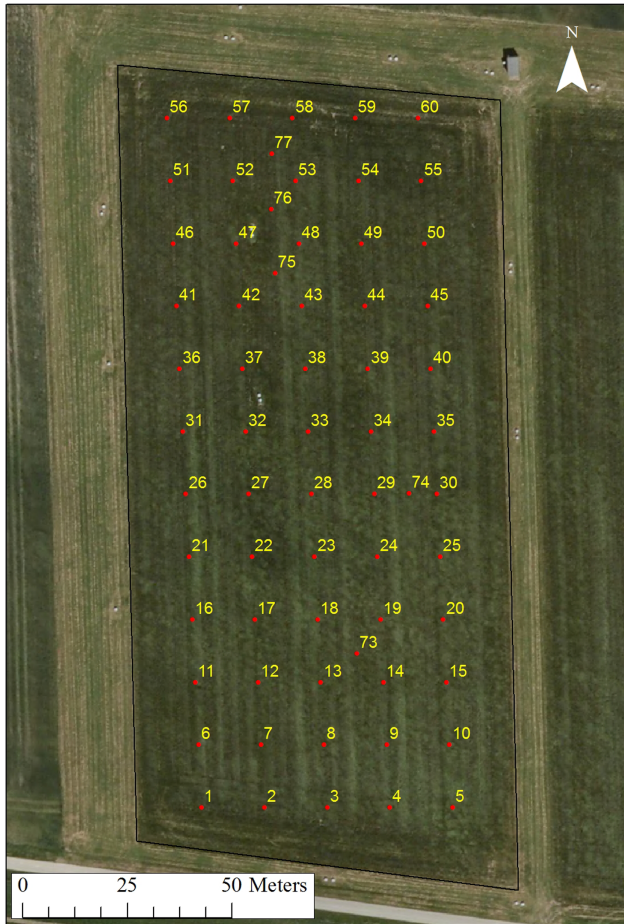


Figure 1. The Silstrup field site with sampling locations. The spacing between the samples from the regular sampling grid is approximately 15 m.

March 2009. On 4 April 2009, slurry had been injected to a depth of 10 cm and to a depth of 4–5 cm in September 2009. In October 2010, 65 undisturbed columns (height 17.2–20 cm, diameter 20 cm) were collected from the topsoil. At the time of sampling the field was cultivated with red fescue (*Festuca rubra* L.). The majority of the sampling locations were arranged in an equidistant grid with a spacing of 15 m covering an area of approximately 1 ha. The exact sampling locations are shown in Figure 1. The sampling points in the grid were placed either at the grid intersects or 1 m away from the grid intersects in random directions, avoiding wheel tracks. This was also done because the sampling grid was aligned with the plow direction and plowing is expected to cause periodical bias [Koestel *et al.*, 2009; Petersen *et al.*, 1997] in soil

Table 2. Texture Fractions Investigated in Our Study and the Corresponding Abbreviations and Definitions

Texture Fraction	Abbreviation	Range of Effective Grain Sizes
Clay	C_{tot}	$<2 \mu\text{m}$
Fine silt	fU	$2\text{--}20 \mu\text{m}$
Coarse silt	cU	$20\text{--}50 \mu\text{m}$
Silt	U_{tot}	$2\text{--}50 \mu\text{m}$
Very fine sand	vfS	$50\text{--}63 \mu\text{m}$
Fine sand	fS	$63\text{--}125 \mu\text{m}$
Medium sand	mS	$125\text{--}200 \mu\text{m}$
Coarse sand	cS	$200\text{--}500 \mu\text{m}$
Very coarse sand	vcS	$500\text{--}2000 \mu\text{m}$
Sand	S_{tot}	$50\text{--}2000 \mu\text{m}$

properties that we sought to avoid. The columns were pushed into the topsoil with a hydraulic press from a tractor until the edge of the column was level with the soil surface. The columns were carefully excavated by hand, trimmed and sealed with plastic caps, and brought to the laboratory. The texture of bulk soil samples was determined according to Gee and Or [2002] by a combined sieve and hydrometer method. Eight texture fractions were determined (Table 2). In addition, the silt and sand fractions were lumped into superclasses (U_{tot} and S_{tot}) whose grain-size boundaries correspond to the ones defined by the USDA. The organic carbon content OC was determined on a LECO analyzer coupled with an infrared CO_2 detector (Thermo Fisher Scientific Inc., USA). It was recently hypothesized that the ratio between the clay content C_{tot} and organic carbon content OC is a fundamental control of the structure of the agricultural topsoil and therefore also for the soil solute transport properties [Dexter *et al.*, 2008; de Jonge *et al.*, 2009]. In the following, we refer to it as the n -index n_D . We also calculated the organic matter content OM from the organic carbon content OC, assuming a conversion factor of 1.7. The bulk density ρ (g cm^{-3}) was determined from the weights of the columns before and after drying at 105°C . The soil porosity φ ($\text{cm}^3 \text{cm}^{-3}$) was estimated from the bulk density ρ assuming the average densities of 2.7 and 1.47 g cm^{-3} for the solid soil mineral and organic phases, respectively. Supplementary information about the Silstrup field site, soil and column handling, and additional analysis carried out during the column leaching experiments can be found in Norgaard *et al.* [2012].

2.2. Breakthrough Experiments

[10] Prior to the BTC experiments, the 65 columns were saturated from the bottom using artificial soil water (see Table 3) for approximately 3 days and then drained through a ceramic plate to a matrix potential of -10 cm at the base of the column (approximately 3 days). The columns were

Table 3. Specifications of the Water Used for Saturating and Irrigating the Soil Columns

	NaCl (mM)	KCl (mM)	CaCl_2 (mM)	MgCl_2 (mM)	pH	Electrical Conductivity (mS cm^{-1})
Artificial soil solution	0.652	0.025	1.842	0.255	6.38	0.6
Artificial rain water	0.121		0.012	0.015	5.76–7.26	0.0225–0.027

then placed on a steel grid with a mesh size of 1 mm. No suction was applied to the lower boundary. The columns were irrigated with artificial rain water (see Table 3) with an intensity of 1 cm h^{-1} from a rotating irrigation head equipped with 44 needles placed randomly to ensure a homogenous application. No ponding was observed during the onset of the experiments except for column 60, where the ponding height remained minimal and no overflow occurred. The effluent was collected through a funnel leading down to 24 plastic bottles rotating automatically. After steady-state flow had been established, a 10 min pulse of tritium-spiked (on average 957.58 kBq/L) artificial rainwater was applied. The effluent was collected in the plastic bottles on the turntable at sampling intervals of 10–30 min. The effluent samples were analyzed for their tritium concentration using liquid scintillation (TRI-CARB 2250 CA). After the breakthrough experiments, the volumetric water contents θ ($\text{cm}^3 \text{ cm}^{-3}$) attained during steady-state flow were determined by weighing the wet and air-dried soil columns. The water saturation S (cm cm^{-3}) was defined as the ratio between the volumetric water content θ and the soil porosity φ . Note that the here presented water saturation S is only a proxy for the true water saturation since the water content θ but not the soil porosity φ was explicitly measured.

2.3. Deconvolution of the BTCs

[11] We first assigned the average time of two consecutive measurements t_{m-1} and t_m to the radioactivity C (kBq/L) detected at t_m :

$$t = \frac{t_{m-1} + t_m}{2}. \quad (1)$$

[12] This corresponds to approximating the change in tritium concentration between the two measurements as being linear. Next, we inserted virtual measurements with a temporal discretization of $dt=0.033 \text{ h}$ (2 min). The respective tritium concentrations C were obtained by linear interpolation between each two consecutive measurements. The insertion of the virtual measurements was included to constrain the deconvolution of the BTC which is described in the following.

[13] We numerically fitted the convolution integral

$$\frac{C(t)}{C_0} = \int_0^t \frac{C_{\text{in}}(t-\tau)}{C_0} f(\tau) d\tau, \quad (2)$$

where C_0 (kBq/L) is the radioactivity of the tracer pulse in the irrigation water, C_{in} (kBq/L) is the time series of the radioactivity in the irrigation water which is C_0 during the first 10 min of each BTC experiment and zero for the remaining time. Furthermore, t (h) and τ (h) are time variables, and f (h^{-1}) is the transfer function [Jury and Roth, 1990], also denoted as the transport-time probability density function (PDF) in the following. We applied a mixture of two log-normal distribution functions [see Koestel et al., 2011] to estimate f according to

$$f(t) = k(w_1 g_1(t) + w_2 g_2(t)), \quad (3)$$

where w_1 and w_2 are the weighting factors that sum up to one, and g_1 (h^{-1}) and g_2 (h^{-1}) are the log-normal distribution functions of the form

$$g(t) = \frac{1}{\sqrt{2\pi}\sigma t} \exp\left[-\frac{(\ln t - \mu)^2}{2\sigma^2}\right], \quad (4)$$

where μ is the log-normalized mean, σ is the log-normalized standard deviation of g , and k is a correction factor for the tracer mass, which depends not only on the mass balance error but also on the temporal discretization dt .

2.4. Evaluation of the Solute BTCs

[14] First, we forward modeled the parameter sets obtained from fitting equation (2) to the data with a temporal discretization of $10^{(-15, -15.05, -15.1, \dots, 14.95, 15)} \text{ h}$. Next, we set all the values of the PDFs $f(t)$ corresponding to an effluent concentration smaller than the detection limit, namely, $C(t)C_0^{-1} < 0.001$, to zero. We then numerically derived five nonparametric BTC shape measures from the reconstructed transfer functions [Koestel et al., 2011]. In the following we give a short overview of the investigated shape measures. A more detailed description of how the five shape measures are calculated is given by Koestel et al. [2012]. First, we calculated the (nonparametric) average transport velocity v (cm h^{-1}) and the apparent dispersivity λ_{app} (cm). The former is defined as the ratio of the column length L (cm) to μ'_1 , the normalized first moment of f , i.e., the arithmetic mean of the transport time. The latter is calculated as

$$\lambda_{\text{app}} = \frac{\mu_2 L}{2(\mu'_1)^2}, \quad (5)$$

where μ_2 is the second central moment of f , i.e., the variance of the transport time; and the ratio of $\sqrt{\mu_2}$ and μ'_1 is the coefficient of variation of f [Jury and Roth, 1990]. The temporal moments of the PDFs $f(t)$ were obtained by using the trapezoidal rule.

[15] We also calculated the ratio of the piston-flow velocity to the average transport velocity which is here denoted as η :

$$\eta = \frac{q}{v\theta}, \quad (6)$$

where q is the water flow rate, and θ is the volumetric water content, and v (cm h^{-1}) is the average tracer velocity, which is defined by $L(\mu'_1)^{-1}$. Note that the definition of the mobility index MI [Lennartz et al., 1997] and piston-flow-to-transport-velocity ratio η is formally identical. What distinguishes η as defined here from MI is the fact that different types of transfer functions were used to fit the data: Lennartz et al. [1997] used the transfer function corresponding to the CDE, whereas we used a double log-normal transfer function.

[16] The fourth and fifth shape measures investigated in this study are the relative arrival time of the first 5% of the tracer mass $p_{0.05}$ and the holdback H . As calculating these two shape measures requires a good temporal resolution

between $0.01\mu'_1 < t < \mu'_1$, we forward-modeled $f(t)$ a second time, this time with a resolution of 0.033 h (2 min).

[17] The relative 5%-arrival time is derived from the normalized arrival times T ,

$$T = \frac{t}{\mu'_1}, \quad (7)$$

and the normalized transport-time PDF, denoted as f_n ,

$$f_n(t) = f(t)\mu'_1. \quad (8)$$

[18] The relative arrival time of the first 5% of the tracer $p_{0.05}$ is calculated from the cumulative distribution function (CDF) F_n which is obtained by integrating f_n ,

$$F_n(T) = \int_0^T f_n dT, \quad (9)$$

as such that

$$F_n(p_{0.05}) = 0.05. \quad (10)$$

[19] The 5% arrival time $p_{0.05}$ is negatively correlated with the strength of preferential transport [Knudby and Carrera, 2005].

[20] Another shape measure for the degree of preferential transport is the holdback factor H defined as the volume of tracer-free water which is still in the soil column after the passage of one effective water-filled pore volume. It was introduced by Danckwerts [1953] but has only been infrequently applied in the soil science community by Rose [1973]. In contrast to $p_{0.05}$, the holdback H is positively correlated with the strength of preferential transport. Koestel et al. [2012] found that H resolves strong to very strong preferential transport well but offers less resolution than $p_{0.05}$ when preferential solute transport is weaker. In this sense, $p_{0.05}$ and H complement each other, whereas $p_{0.05}$ has the advantage that it appears to be more robust to the choice of transfer function type used in equation (2) [Koestel et al., 2011].

2.5. Spatial Interpolation

[21] We interpolated the soil properties, the hydrologic state variables, and the BTC shape measures to facilitate visual recognition of spatial patterns. The sampling distance was approximately 15 m. It follows that the interpolated images only show heterogeneities larger than this distance, i.e., the sampling distance acts as a low-pass filter. We advise the reader against interpreting the data between the sampling points as known. As the sampling grid used in this study is slightly distorted in the X direction, linear or nearest neighbor interpolations lead to interpolations that falsely suggest undulating patterns aligned to the sampling grid distortions. We therefore used natural neighbor interpolation [Sibson, 1981] which resulted in a more isotropic representation of the sampled data. Finally, we calculated semivariograms [Christakos, 2000] for all predictors, hydrologic state variables, and BTC shape measures for estimating the respective correlation lengths.

2.6. Regression Analyses

[22] We built simple predictive relationships for the five shape measures using linear ridge regressions with the available texture data, i.e., C_{tot} , U_{tot} , fU , cU , S_{tot} , vfS , fS , mS , cS , and vcS (Table 2), the organic matter content OM , the n -index n_D , and the bulk density ρ as predictors. Prior to evaluating the regression functions, the predictors were normalized to their respective means and standard deviation. If the corresponding shape measure was log-normal distributed, the logarithmized values were estimated rather than the original value.

[23] We first applied a bootstrap approach to select predictor subsets as promising candidates for the ridge regressions. This step was included to identify weak predictors with little contribution to the regression. Excluding the weak predictors greatly shortened and simplified the final regression functions without significantly reducing their performance. For each bootstrap sample n_{BS} we carried out a forward-stepwise predictor selection. In each step we added or dropped the predictor which minimized the Akaike information criterion (AIC) until a local minimum was reached [Hastie et al., 2009]. In this fashion a best-subset regression function was obtained for each bootstrap sample. The performance of each regression function was appraised by the leave-one-out (LOO) error. The 25 regression functions with the smallest LOO errors were selected for ridge regression, thereby implementing a nongreedy subset selection. The bootstrap approach was also used for appraising the importance of each of the 13 predictors. This was quantified as the percentage of all (bootstrap) regression functions for which the predictor was retained.

[24] Ridge regression is a shrinkage method which trades bias for variance, i.e., the predictive relationships obtained are slightly biased but more robust against outliers, or in other words, overfitting is prevented by imposing a smoothness constraint on the regression [Hastie et al., 2009]. It has the form

$$\mathbf{y} = \mathbf{X}\mathbf{b} + b_0\mathbf{I}, \quad (11)$$

where $\mathbf{y} = (y_1, y_2, y_3, \dots, y_m)^T$ is the vector of the target variable, i.e., either one of v , λ_{app} , $p_{0.05}$, H , or η , for the m data sets; \mathbf{X} is an $m \times n$ matrix of the n normalized predictor vectors $\mathbf{x}_n = (x_{1,n}, x_{2,n}, x_{3,n}, \dots, x_{m,n})^T$ which contain m data sets corresponding to the size of one bootstrap sample; $\mathbf{b} = (b_1, b_2, b_3, \dots, b_n)^T$ is the vector of the n regression coefficients; \mathbf{I} is the $n \times n$ identity matrix; and b_0 is the intercept which is set to the mean value of \mathbf{y} . For ridge regression the regression coefficients \mathbf{b} are calculated as

$$\mathbf{b} = (\mathbf{X}^T\mathbf{X} + \alpha\mathbf{I})^{-1}\mathbf{X}^T\mathbf{y}, \quad (12)$$

where α is the penalty term which determines the degree of shrinking applied to the regression. The penalty term α was determined by fivefold cross validation. The final regression functions were found by applying equation (12) to the complete data set with the size $m=65$, using the 25 best predictor subsets that had been identified during bootstrapping. Out of these 25 regression functions (25 for each investigated shape measure), the one with the smallest AIC

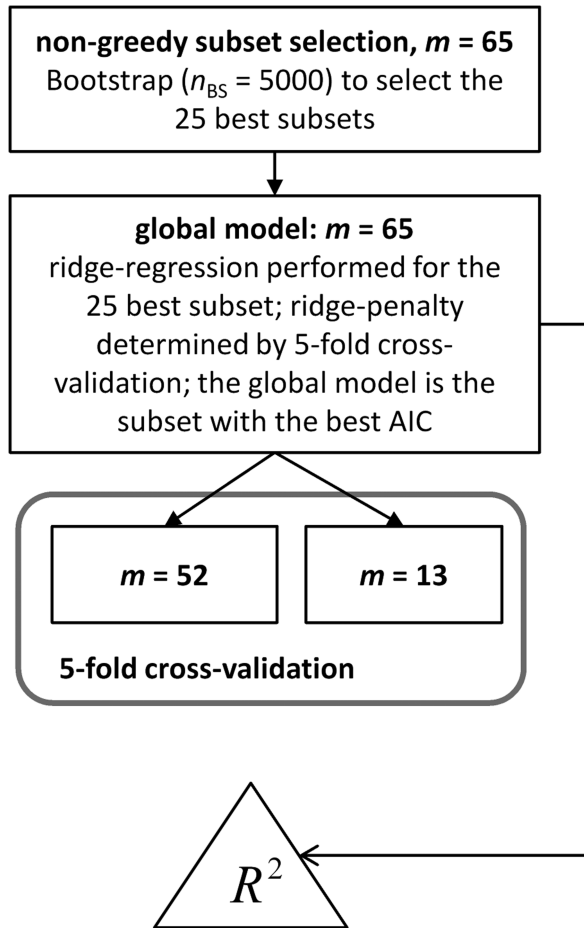


Figure 2. A scheme illustrating the parameterization and validation approach used for the regression relationships.

was selected. Figure 2 illustrates the above described approach.

2.7. Upscaling of the Column-Scale BTCs to the Field Scale

[25] We numerically upscaled the column-scale normalized PDFs $f_n^{(m)}(t)$ to the field-scale PDF $u_n(t)$ by taking the arithmetic mean of all m ($=65$) data sets:

$$u_n(t) = \frac{\sum_1^m f_n^{(m)}(t)}{m}. \quad (13)$$

[26] As the irrigation rate was constant for all columns and ponding was negligible, weighting of the normalized PDFs $f_n^{(m)}(t)$ by the water flux can be dispensed with. The upscaling approach assumes that each column-scale BTC was representative for the area in the field where the column had been collected. Each area would correspond to approximately 0.015 ha (65^{-1} ha). It should also be noted that the upscaling approach only approximates the field-scale transport characteristics with respect to the lateral scale. The upscaled PDF is therefore only an estimate for the field-scale solute transport through the topsoil.

[27] The field-scale shape measures were derived from $u_n(t)$ as described in section 2.2. We applied the regression relationships obtained for the local-scale BTC shape

measures on the arithmetic mean soil properties to obtain estimates of the field-scale shape measures. The deviations between the shape measures from the upscaled PDF $u_n(t)$ and the estimated shape measures were discussed.

3. Results and Discussion

3.1. Soil Properties and Hydraulic State Variables

[28] Figure 3a shows that the Silstrup field site exhibits a slight gradient in the clay content C_{tot} with a larger clay content (approximately 0.18 g g^{-1}) in the northern half of the investigated area than in the southern half (approximately 0.15 g g^{-1}). The total sand fraction S_{tot} and the total silt fraction U_{tot} are relatively constant between 0.5 and 0.53 g g^{-1} and 0.29 and 0.33 g g^{-1} , respectively (Figures 3b and 3c). The only major variation in the total sand content S_{tot} is observed in the northwestern area of the field where it varies between 0.45 and 0.55 g g^{-1} and is negatively correlated with the clay content. For the total silt content U_{tot} there were only two sampling locations in the north of the investigated area where it was slightly smaller with the values of 0.24 g g^{-1} . The bulk density varies between 1.4 and 1.6 g cm^{-3} (Figure 4a). The regions with lower bulk density are located in the center of the investigated field. The organic matter is distributed relatively homogeneously and varies between 0.029 and 0.037 g g^{-1} with its minima and maxima neighboring in the northwestern quadrant of the field (Figure 4b). The pattern of the n -index n_D follows the distribution of the clay content with larger values in the northern than in the southern half of the field (Figure 4c).

[29] Figure 5 depicts the distribution of the volumetric water content θ and the degree of saturation S under the experimental conditions during the tracer experiments, i.e., steady-state irrigation of 1 cm h^{-1} . The water content θ varied between 0.38 and $0.43 \text{ cm}^3 \text{ cm}^{-3}$, and its pattern exhibited little resemblance to the soil properties discussed above. The water saturation S , however, closely followed the distribution of the bulk density ρ . All soil columns were close to the water saturation ($S > 0.84$). In approximately half of them the water saturation exceeded 0.93. The water content θ and the water saturation S are shown in Table 4.

3.2. Column-Scale BTCs

[30] Figure 6 shows the four examples of the BTCs with the respective fits of the transfer function (see equations (1)–(4)) as well as the corresponding transport-time PDFs and CDFs. Bimodal BTCs like the one sampled from column 29 were only observed in three cases. The column-scale BTC shape measures are listed in Table 4. The histograms of three of the considered BTC shape measures, namely, the column-scale velocity v , and apparent dispersivity λ_{app} , and the 5% arrival time $p_{0.05}$, resembled log-normal distributions, whereas the histogram of the piston-flow-to-transport-velocity ratio η and the holdback H were quasi-normally distributed (not shown).

[31] The spatial patterns of all the five investigated shape measures (Figure 7) followed the spatial distributions of the bulk density ρ (Figure 4) and the water saturation S (Figure 5b). The piston-flow-to-transport-velocity ratio η varied between 0.19 and 1.41. The median of 0.92 indicates that the tracer was accelerated relative to the water flow in

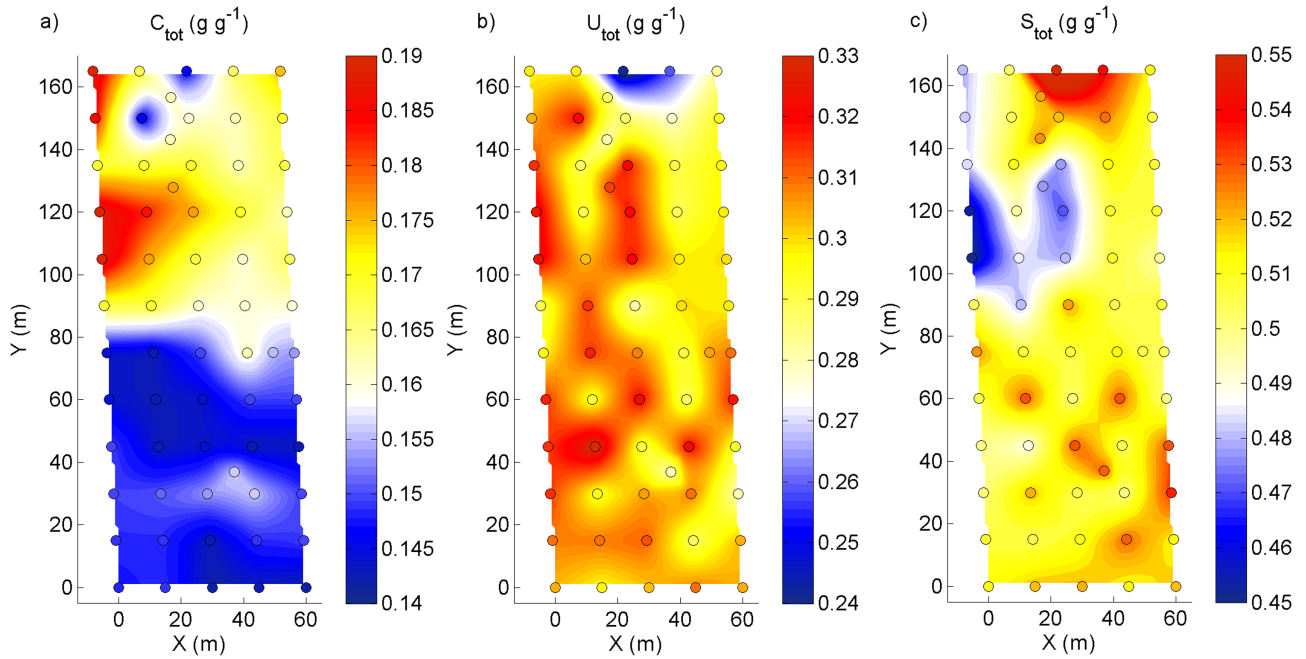


Figure 3. The soil texture fractions according to the USDA: (a) the total clay fraction C_{tot} ($<2 \mu\text{m}$), (b) the total silt fraction U_{tot} ($2 < U < 50 \mu\text{m}$), and (c) the total sand fraction S_{tot} ($>50 \mu\text{m}$).

the majority of the soil columns. This may be explained by preferential flow which caused bypassing of the tracer of a considerable fraction of the pore space [e.g., *Vanderborght and Vereecken, 2007*]. The values of η were clearly larger than the values of the mobility index MI reported by *Lennartz et al. [1997]*. However, just the fact that *Lennartz et al. [1997]* used a different transfer-function type than in

our study makes it difficult to relate η and MI. Furthermore, it has to be taken into account that *Lennartz et al. [1997]* used an anionic tracer which favors bypassing of pore space due to anion exclusion [*Thomas and Swoboda, 1970; Rose et al., 2009*].

[32] The occurrence of preferential flow is supported by the relatively large apparent dispersivities λ_{app} (median of

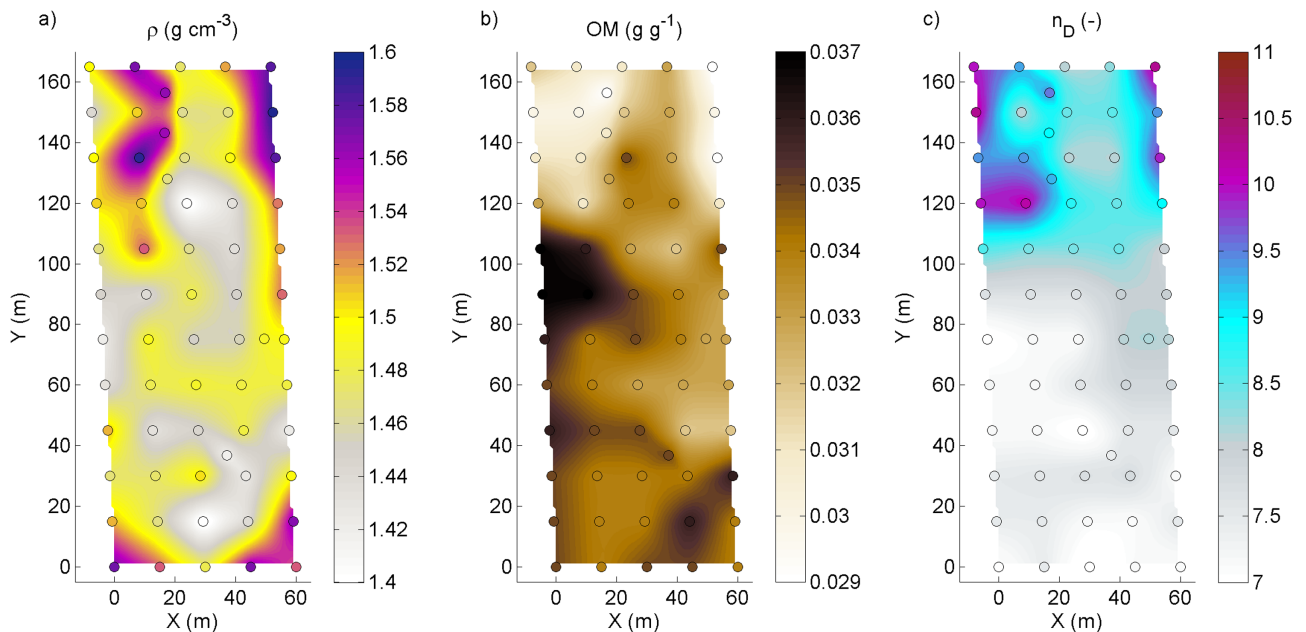


Figure 4. (a) The soil bulk density ρ , (b) the soil organic matter content OM, and (c) the ratio between the clay content and the organic carbon n_D .

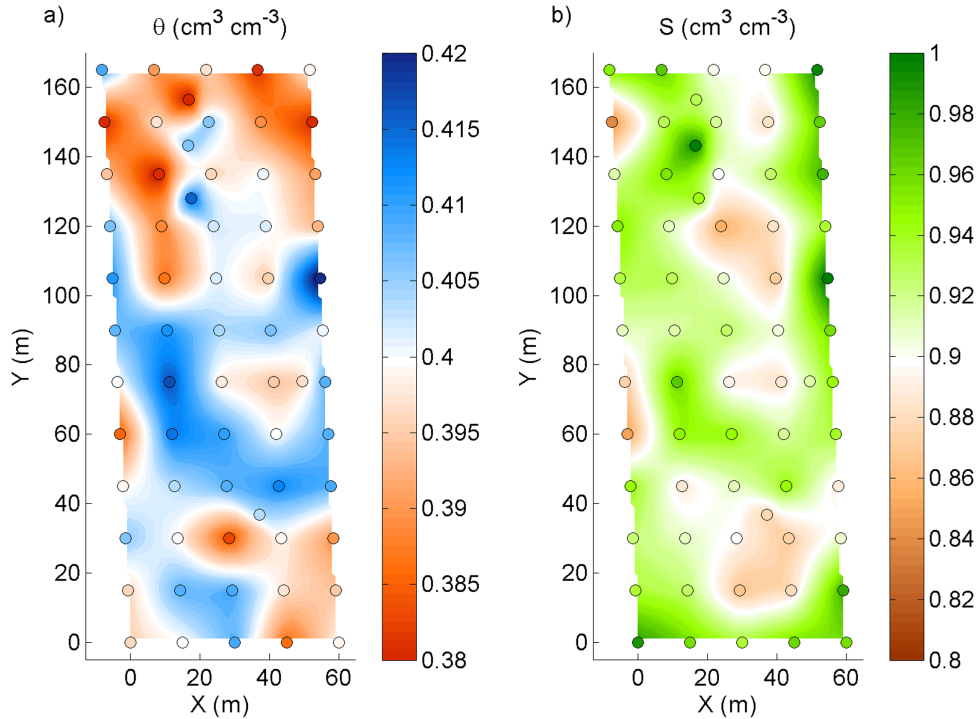


Figure 5. (a) The volumetric water content θ and (b) the water saturation S .

19.28 cm) and also by the 5% arrival times $p_{0.05}$ and the holdback factors H . Both $p_{0.05}$ and H indicated a strong preferential transport (Figures 7d and 7e). The 5% arrival time $p_{0.05}$ in our study had a median value of 0.08, which was clearly below the median $p_{0.05}$ found for undisturbed soil in the meta-analysis of Koestel *et al.* [2012], which was approximately 0.25. If a $p_{0.05}$ of less than 0.25 is chosen as a threshold for preferential transport, then only one column did not exhibit preferential transport (column 73 which yielded a $p_{0.05}$ of 0.35).

3.3. Correlations Among Soil Properties, Hydraulic State Variables, and BTC Shape Measures

[33] The observed similarity between the patterns of water saturation S and all investigated BTC shape measures was consistent with large mutual correlation coefficients (Figure 8). The correlations were such that with increasing S , the tracer arrived earlier, the effective water content decreased, and the spread of the BTCs became larger. Figure 8 shows that mainly five soil properties were significantly correlated with the investigated BTC shape measures. These were the bulk density ρ , the fractions of very fine sand vfS and very coarse sand vcS, the organic matter OM, and the n -index n_D . The spatial distributions of the two sand fractions are depicted in Figure 9. The bulk density ρ exhibited the strongest correlations with the BTC shape measures with absolute values between 0.44 and 0.67 and was positively correlated with the strength of preferential transport. Notably, ρ was also very strongly correlated with the water saturation S ($r=0.82$). The very fine sand fraction vfS was only significantly correlated with λ_{app} , $p_{0.05}$, and H and in contrast negatively correlated with the strength of preferential transport with absolute Spear-

man rank correlation coefficients between 0.36 and 0.42. Its correlation coefficient with the water saturation was -0.44 . The very coarse sand fraction vcS was positively correlated with the transport velocity v ($r=0.47$) and negatively with the piston-flow-to-transport-velocity ratio η ($r=-0.47$), i.e., the transport was by trend accelerated in the columns containing larger amounts of very coarse sand. The opposite was observed for the column with larger organic matter contents OM (Figure 8), with Spearman correlation coefficients of -0.41 and 0.4 , respectively. Notably, OM was negatively correlated with the very coarse sand fraction vcS with a Spearman correlation coefficient of -0.52 . The correlations of the n -index n_D with the transport velocity v and the piston-flow-to-transport-velocity ratio η were opposite to the ones found for OM (Figure 8). This is consistent with the fact that no correlation between the clay content C_{tot} and any shape measure was observed as n_D is defined as the ratio between clay content and organic carbon content.

[34] In conclusion, the water saturation S was under the experimental conditions of steady-state irrigation of 1 cm h^{-1} strongly correlated with the bulk density ρ . The water saturation S was, in turn, significantly positively correlated with the strength of preferential transport. The relationship among the bulk density ρ , the water saturation S , and the strength of preferential transport portrayed by the holdback H is also illustrated in Figure 10. It can be seen that the spatial distributions of ρ , S , and H roughly matched. An intuitive explanation for the observed correlations is the following: the bulk density was related to reductions of the near-saturated hydraulic conductivity, which lead to larger water saturations under the constant water flow rate of 1 cm h^{-1} and to the activation of larger macropores and

Table 4. Volumetric Water Contents θ , Water Saturation S , Transport Velocities v , Apparent Dispersivity λ_{app} , Relative 5%-Arrival Time $p_{0.05}$, Holdback H , Ratio Between Piston-Flow and Transport Velocity η , Coefficient of Determinations From Fitting the Transfer Functions to the Data, and Mass Balance (MB).

Col. Number	θ (cm ³ cm ⁻³)	S	v (cm h ⁻¹)	λ_{app} (cm)	$p_{0.05}$	H	η	R^2	MB (%)
1	0.40	0.99	13.41	65.48	0.04	0.56	0.19	1.00	116.71
2	0.40	0.96	3.38	55.45	0.04	0.62	0.74	0.99	113.40
3	0.41	0.94	2.14	19.87	0.07	0.45	1.14	1.00	114.06
4	0.39	0.96	5.17	33.39	0.07	0.52	0.50	1.00	117.65
5	0.40	0.96	2.20	35.81	0.03	0.56	1.14	1.00	111.33
6	0.40	0.94	5.55	17.47	0.11	0.43	0.45	1.00	95.42
7	0.41	0.93	3.35	6.06	0.15	0.29	0.73	1.00	100.19
8	0.41	0.87	2.29	10.42	0.16	0.33	1.07	1.00	103.83
9	0.40	0.88	1.97	16.39	0.09	0.39	1.28	0.97	104.58
10	0.39	0.98	2.03	36.97	0.03	0.56	1.25	1.00	109.21
11	0.41	0.92	2.09	28.42	0.04	0.53	1.18	1.00	105.79
12	0.40	0.91	2.26	19.67	0.07	0.46	1.11	1.00	104.60
13	0.38	0.90	2.26	40.55	0.03	0.59	1.16	1.00	100.81
14	0.40	0.87	2.03	23.97	0.05	0.49	1.23	1.00	107.16
15	0.39	0.91	2.05	29.65	0.05	0.52	1.25	1.00	111.50
16	0.40	0.95	2.35	39.88	0.04	0.58	1.07	1.00	109.42
17	0.40	0.89	2.08	13.83	0.09	0.40	1.19	0.99	88.40
18	0.41	0.91	2.34	11.99	0.12	0.38	1.05	1.00	77.63
19	0.41	0.95	2.17	16.73	0.09	0.42	1.11	1.00	103.77
20	0.41	0.89	2.77	9.45	0.13	0.34	0.88	1.00	93.57
21	0.39	0.85	2.85	13.81	0.09	0.39	0.91	0.99	105.97
22	0.41	0.95	4.35	7.08	0.12	0.31	0.56	0.99	116.29
23	0.41	0.95	4.03	15.89	0.10	0.42	0.60	1.00	95.58
24	0.40	0.92	3.43	15.76	0.10	0.41	0.73	1.00	103.20
25	0.41	0.94	2.36	29.48	0.04	0.52	1.04	1.00	113.21
26	0.40	0.87	2.52	8.75	0.18	0.33	0.99	1.00	112.02
27	0.42	0.97	2.01	16.93	0.08	0.44	1.19	1.00	105.93
28	0.40	0.89	2.85	15.83	0.10	0.42	0.88	1.00	117.36
29	0.39	0.88	3.35	5.25	0.10	0.28	0.76	0.98	88.38
30	0.41	0.94	2.67	24.48	0.06	0.49	0.92	1.00	106.30
31	0.41	0.91	1.76	33.53	0.03	0.56	1.39	1.00	108.55
32	0.41	0.91	1.98	18.08	0.07	0.44	1.22	1.00	108.48
33	0.40	0.93	3.13	13.63	0.09	0.41	0.79	1.00	109.69
34	0.41	0.91	1.75	26.17	0.04	0.52	1.41	1.00	107.27
35	0.40	0.96	2.29	19.28	0.06	0.46	1.09	1.00	114.62
36	0.41	0.93	1.86	37.47	0.02	0.58	1.31	1.00	108.79
37	0.39	0.93	3.02	18.99	0.08	0.45	0.86	1.00	113.14
38	0.40	0.91	3.06	11.96	0.13	0.38	0.81	1.00	107.41
39	0.40	0.87	2.36	11.52	0.11	0.36	1.07	1.00	117.00
40	0.43	1.01	1.83	46.30	0.02	0.62	1.28	1.00	105.84
41	0.41	0.95	4.74	21.88	0.08	0.47	0.52	1.00	100.79
42	0.39	0.91	3.01	20.50	0.07	0.46	0.86	1.00	93.74
43	0.40	0.85	4.56	9.55	0.13	0.37	0.55	1.00	92.55
44	0.40	0.88	2.37	10.56	0.13	0.36	1.05	1.00	104.60
45	0.39	0.94	3.38	36.01	0.06	0.52	0.75	0.99	95.35
46	0.39	0.91	2.58	14.15	0.09	0.40	0.98	1.00	108.03
47	0.38	0.96	4.56	47.84	0.05	0.59	0.58	1.00	106.14
48	0.40	0.90	3.26	22.57	0.08	0.48	0.77	1.00	103.14
49	0.40	0.93	2.45	16.46	0.09	0.43	1.02	1.00	111.33
50	0.39	0.98	5.51	19.44	0.12	0.44	0.46	1.00	100.94
51	0.38	0.84	2.53	8.80	0.16	0.32	1.04	1.00	103.84
52	0.40	0.93	3.29	47.51	0.04	0.62	0.77	1.00	102.08
53	0.41	0.92	2.00	15.52	0.09	0.41	1.23	0.99	113.88
54	0.39	0.88	2.83	8.65	0.15	0.33	0.91	1.00	101.81
55	0.38	0.96	6.06	19.52	0.09	0.45	0.43	1.00	93.85
56	0.41	0.95	2.89	18.60	0.08	0.44	0.85	1.00	105.64
57	0.39	0.97	6.29	23.90	0.08	0.48	0.41	1.00	100.24
58	0.40	0.90	2.94	28.11	0.06	0.51	0.86	1.00	111.99
59	0.38	0.90	5.44	23.87	0.07	0.48	0.48	1.00	93.84
60	0.40	1.00	4.90	60.36	0.03	0.61	0.51	1.00	101.97
73	0.40	0.87	2.70	3.37	0.35	0.22	0.92	1.00	102.07
74	0.40	0.92	2.50	10.90	0.11	0.37	1.01	1.00	113.59
75	0.41	0.94	2.43	11.07	0.05	0.38	0.99	0.98	107.27
76	0.41	1.00	4.36	41.66	0.05	0.56	0.56	1.00	109.06
77	0.38	0.93	3.43	49.60	0.04	0.62	0.77	1.00	101.87
Mean	0.40	0.92	3.21	23.26	0.08	0.45	0.90	1.00	105.13
Harmonic mean	0.40	0.92	2.76	15.89	0.06	0.43	0.78	1.00	104.50
Median	0.40	0.93	2.70	19.28	0.08	0.45	0.92	1.00	105.93
Field scale			2.71	26.73	0.03	0.55	0.92		
Field scale (predicted) ^a			2.94	19.41	0.07	0.45	0.90		

^aThe predicted field-scale shape measures using the arithmetic mean values of the local-scale soil properties and the regression relationships are listed in Table 5.

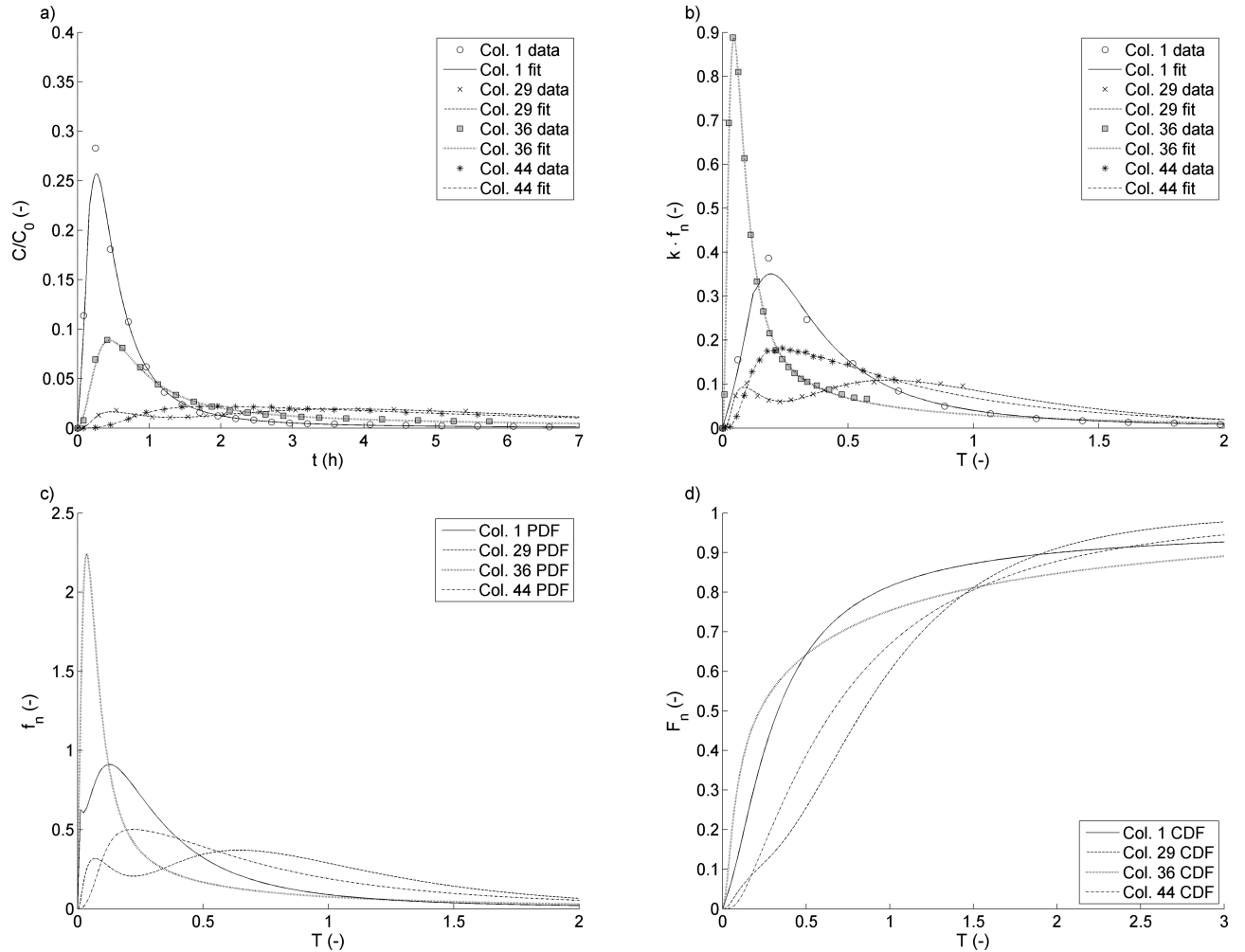


Figure 6. (a) Some example BTCs plotted against the real time in hours, (b) the same BTCs plotted against the effective drained pore volumes, (c) the PDFs corresponding to the BTCs, and (d) the CDFs corresponding to the BTCs.

therefore stronger macropore flow and stronger preferential transport characteristics. A definitive proof of this hypothesis would however require 3-D images of the soil pore space or measurements of the near-saturated hydraulic conductivity which both were not at our disposal.

[35] It is to point out that the meta-analysis of 733 BTC experiments of *Koestel et al.* [2012] yielded a negative correlation between bulk density ρ and the strength of preferential transport. This is in contrast to our results from the Silstrup field site, which strongly suggests that the relationships at the Silstrup site cannot be generalized in a simple fashion for other soils.

[36] Some previous studies have suggested that organic matter may reduce preferential transport in a cultivated topsoil [*Roulier and Jarvis, 2003; Jarvis, 2007*]. By trend, the soil organic matter content was negatively correlated with the transport velocity v and positively correlated with the piston-flow-to-transport-velocity ratio η . Hence, larger organic matter contents supported retardation of tritium. This may be interpreted as a reduction in preferential transport. The same holds for the ratio between clay and organic carbon, n_D , which is also thought to exert an important

control on the aggregate structure developed under cultivation [*de Jonge et al., 2009*]. However, our study provides no evidence that n_D may be a superior indicator for soil susceptibility to retarded transport than OM. It is to note that neither OM nor n_D were significantly correlated with any shape measure related to the spread and earliness of the tracer arrival. This may be due to the fact that the variability of the organic matter content at the Silstrup field site (2.9%–3.7%) was probably too small to lead to significant differences in the respective features of the investigated BTCs. It is moreover a further indication that the piston-flow-to-transport-velocity ratio η carries different information on the solute transport process than λ_{app} , $p_{0.05}$, and H , as already observed by *Koestel et al.* [2012].

[37] The clay content had no directly observable effect on the BTC shapes at Silstrup. However, this is not a contradiction to the empirical notion that the clay content is an important driver of preferential flow and transport. The results of the meta-analysis of *Koestel et al.* [2012] suggest that the occurrence of preferential transport depends in a threshold-like manner on the clay content. They found a threshold of approximately 8% clay above which

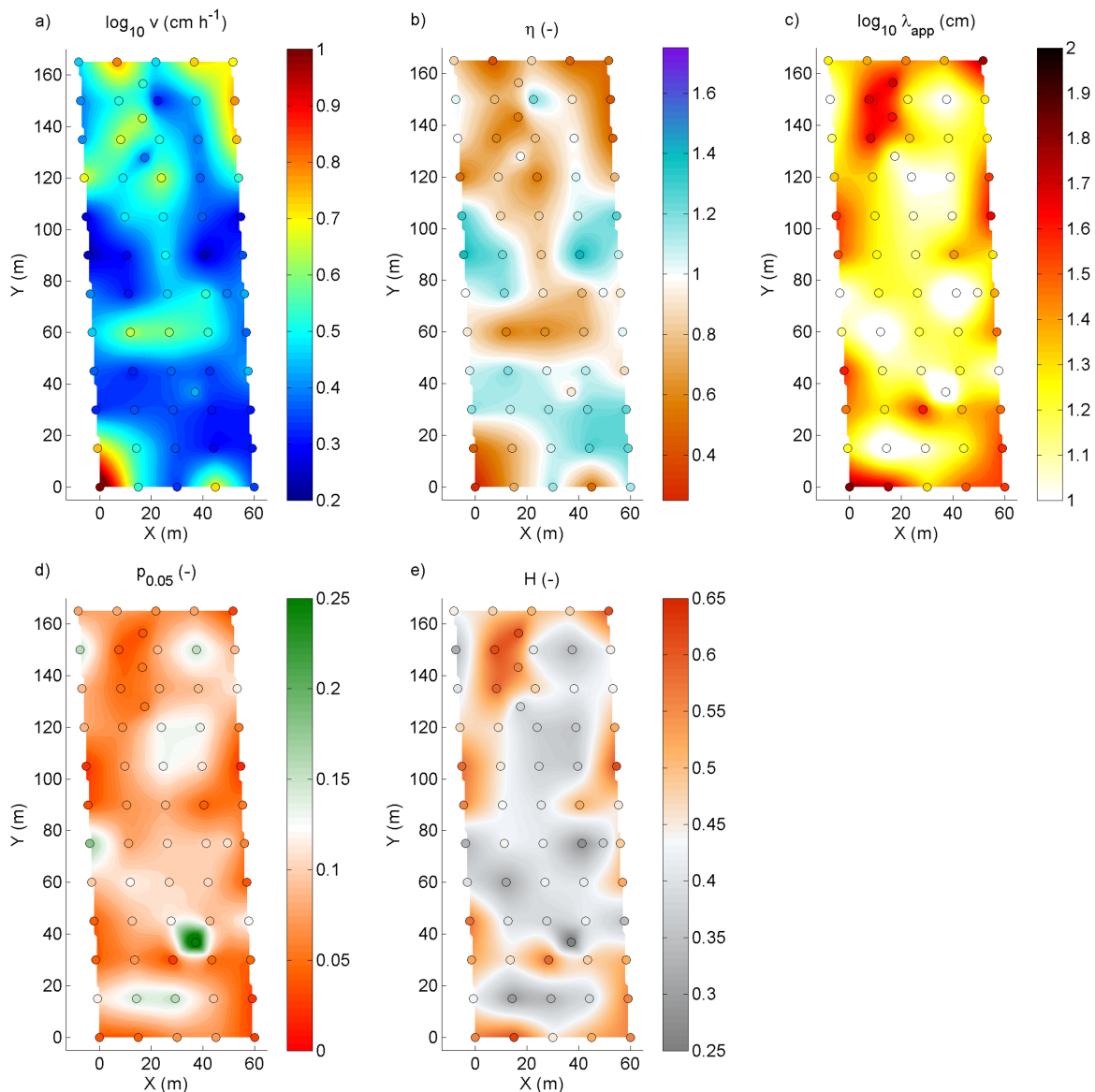


Figure 7. (a) The logarithmized transport velocity v , (b) the piston-flow-to-transport-velocity ratio η , (c) the apparent dispersivity λ_{app} , (d) the relative 5%-arrival time $p_{0.05}$, and (e) the holdback H .

preferential transport was possible. Above this threshold, the strength of preferential transport did not depend linearly on the clay content. Similar thresholds were also reported by *Quisenberry et al.* [1993] and *de Jonge et al.* [2004] for much smaller data sets, at clay contents of 8% and 13%, respectively. These clay contents roughly coincide with that necessary to form stable aggregates [*Horn et al.*, 1994]. As the clay content at Silstrup (14%–19%) was well above these thresholds, we suggest that the strong preferential transport characteristics which can be attributed to almost all investigated BTCs were in part caused by soil aggregation and in part also by the presence of biopores in combination with the an irrigation rate that, lead to water contents close to saturation. Notably, column 73, which was the only column for which preferential transport was not observed, still had a clay content of 15.6% but otherwise possessed soil properties that according to the

observed correlation acted against the promotion of both near-saturated conditions and preferential flow, namely, a small bulk density ρ of 1.42 g cm^{-3} , a large very fine sand fraction vfS (0.074 g g^{-1}), and a small very coarse sand fraction vcS (0.065 g g^{-1}). It should be noted that the bottom boundary condition which was a seepage face leads to saturated conditions near the outflow. Saturated conditions promote preferential transport in general, and the strong preferential characteristics that were found in our study are to an uncertain extent affected by the choice of the bottom boundary condition.

[38] We also investigated the spatial correlation of the predictors and BTC shape measures. Only 4 of the 13 investigated predictor variables had a correlation length larger than the sampling distance (Figure 11a). These were the total clay content C_{tot} , the total sand content S_{tot} , the organic matter content OM , and the very coarse sand content

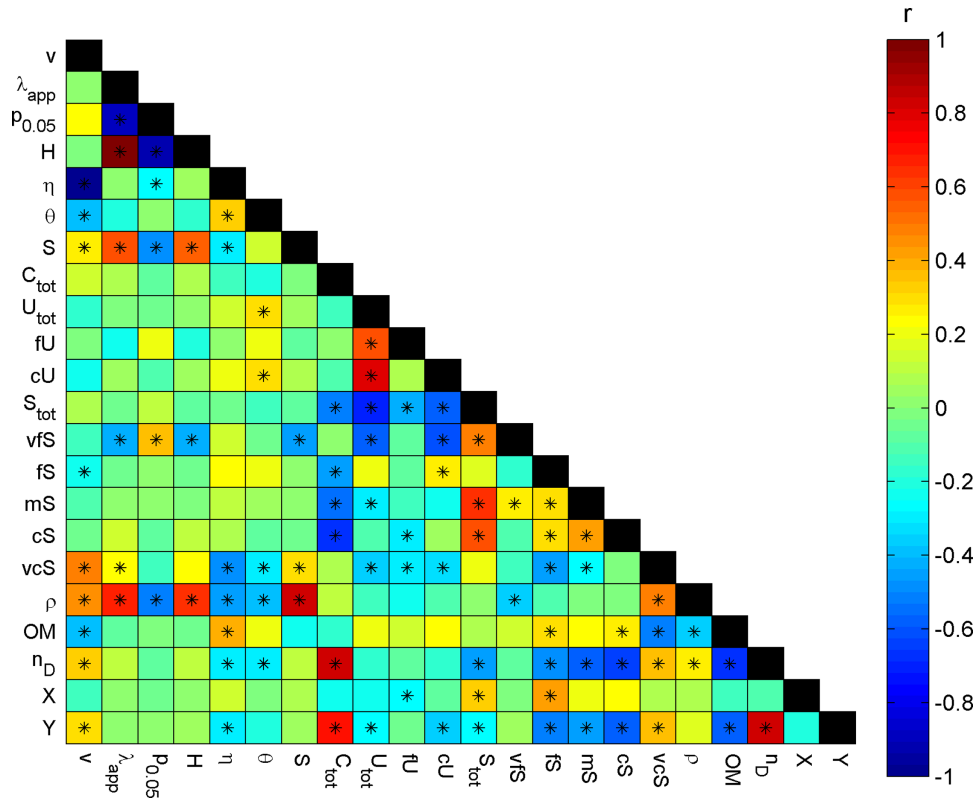


Figure 8. The correlation matrix of the mutual Spearman rank correlation coefficients r . The asterisks indicate the significance with p values smaller than 0.05.

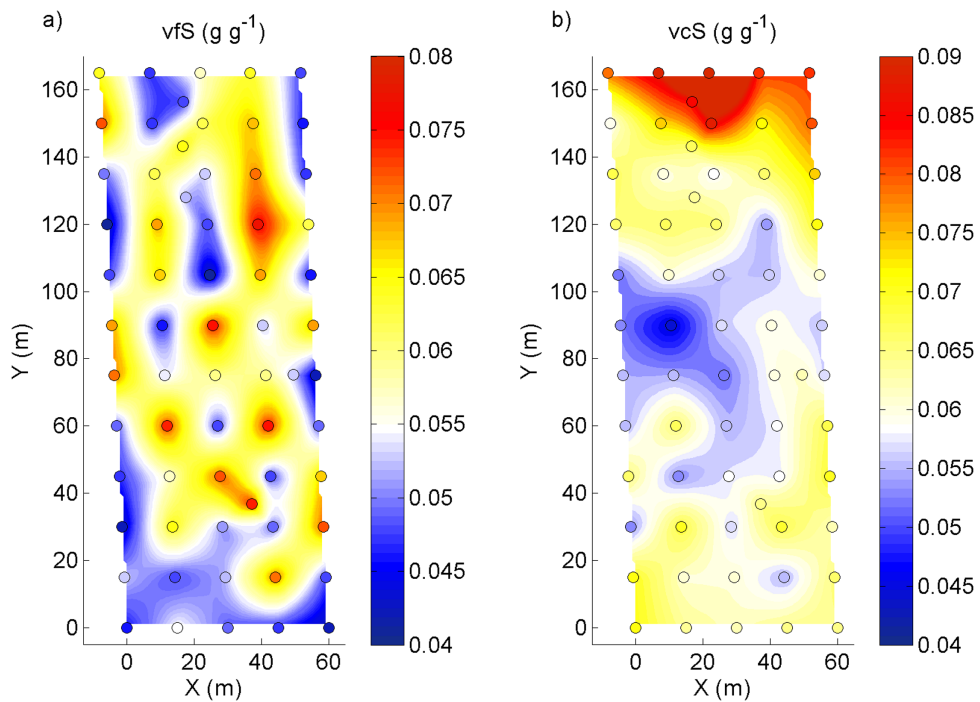


Figure 9. The two sand fractions showing significant correlation with the investigated BTC shape measures: (a) the very fine sand fraction vfS ($50\text{--}63\ \mu\text{m}$) and (b) the very coarse sand fraction vcS ($500\text{--}2000\ \mu\text{m}$).

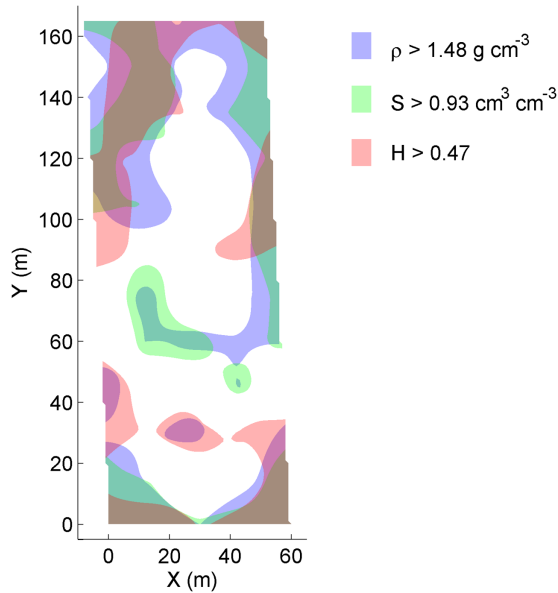


Figure 10. The distribution patterns of the predictor variable bulk density $\rho > 1.48 \text{ g cm}^{-3}$, the state variable water saturation $S > 0.93$, and one of the investigated shape measures, the holdback $H > 0.47$.

vcS. We found that only the sand content S_{tot} exhibited a correlation length within 15 m (sampling distance) and 100 m (average scale the field). It was approximately 50 m (Figure 11a). The nearly linear variograms of the other three soil properties suggest strong trends of the respective soil properties over the Silstrup field site. Of these, only the vcS was significantly correlated with the BTC shape measures, albeit only moderately. It is therefore not surprising that the majority of the BTC shape measures also show correlation lengths of less than 15 m (Figure 11b). Only the transport velocity v and the piston-flow-to-transport-

velocity ratio η had correlation lengths larger than the sampling distance, but they also had a large nugget with a semivariance of $>60\%$ (Figure 11b). We conclude that a better spatial resolution of sampling sites ($<15 \text{ m}$) would be beneficial to fully characterize the spatial dependence of solute transport properties at the Silstrup field site under near-saturated hydraulic conditions.

3.4. Regression Analysis

[39] The results of the bootstrap and regression analyses support the conclusions drawn from the correlation between soil properties and BTC shape measures. All regression equations contained the bulk density (Table 5) which was to be expected given its large correlations to all investigated shape measures. Notably, all regression relationships except the one for the piston-flow-to-transport-velocity ratio η include the very fine or the very coarse sand fraction as a predictor (Table 5). This suggests that more detailed information on the soil texture than the three USDA texture fractions clay, silt, and sand may be useful to predict solute transport properties from soil texture. Table 5 illustrates that the ridge-regression approach yielded the coefficients of determination R^2 between 0.41 and 0.44 for the apparent dispersivity λ_{app} and the holdback H . Taking into account the relatively small variability of soil texture and organic matter content as well as BTC shape measures in this study, a coefficient of determination of larger than 0.4 is still a fairly good result. The transport velocity v , the relative 5% arrival time $p_{0.05}$, and the piston-flow-to-transport-velocity ratio η were less well predicted from the investigated soil properties with R^2 of 0.31, 0.31, and 0.28, respectively.

[40] In the following, we used H in our examples which illustrate typical details for the predictor importance and the regression performance found for the investigated BTC shape measures. Figure 12a depicts the frequency with which each of the 13 predictors were selected as a best subset in the 5000 bootstrap samples used for the nongreedy best-subset evaluation. The more frequent a predictor was

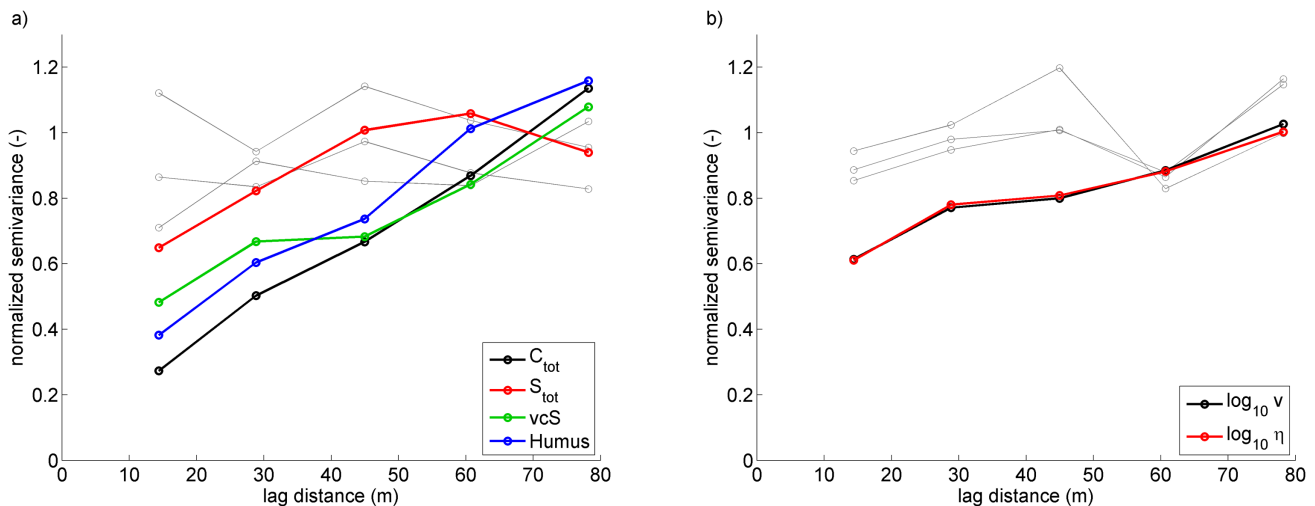


Figure 11. (a) The spatial correlation of the predictors and (b) the shape measures. Only the predictors exhibiting correlation lengths larger than the main sampling distance of 15 m are shown in color.

Table 5. Regression Relationships Between Soil Properties and the Five Investigated BTC Shape Measures Using Ridge Regression^a

Shape Measure	Regression Function	R^2
v	$\exp(-3.3792+2.7645\rho+5.0533vcS)$	0.31
λ_{app}	$\exp(-4.1167+5.1934\rho-11.0835vfS)$	0.44
$p_{0.05}$	$\exp(2.8817-3.3669\rho+10.5808vfS-19.1860OM)$	0.31
H	$-0.5291+0.7297\rho-1.7606vfS$	0.41
η	$2.2342-1.5573\rho+16.8789OM$	0.28

^aIn addition, the respective coefficients of determinations are shown.

selected, the greater was its importance. Figure 12a illustrates that the bulk density ρ was by far the most important predictor, followed by the very fine sand fraction vfS . Consequently, regression functions containing only these two variables also proved to perform best in the cross validation. Figure 12b shows how the function in Table 5 predicts the holdback factor, while Figures 12c and 12d illustrate how it reproduced the spatial pattern of H as compared to the measured values. Finally, Figure 12e shows the respective residuals as a percentage of the measured holdback. Due to the smoothness constraint used in the ridge regression, the maximum values were

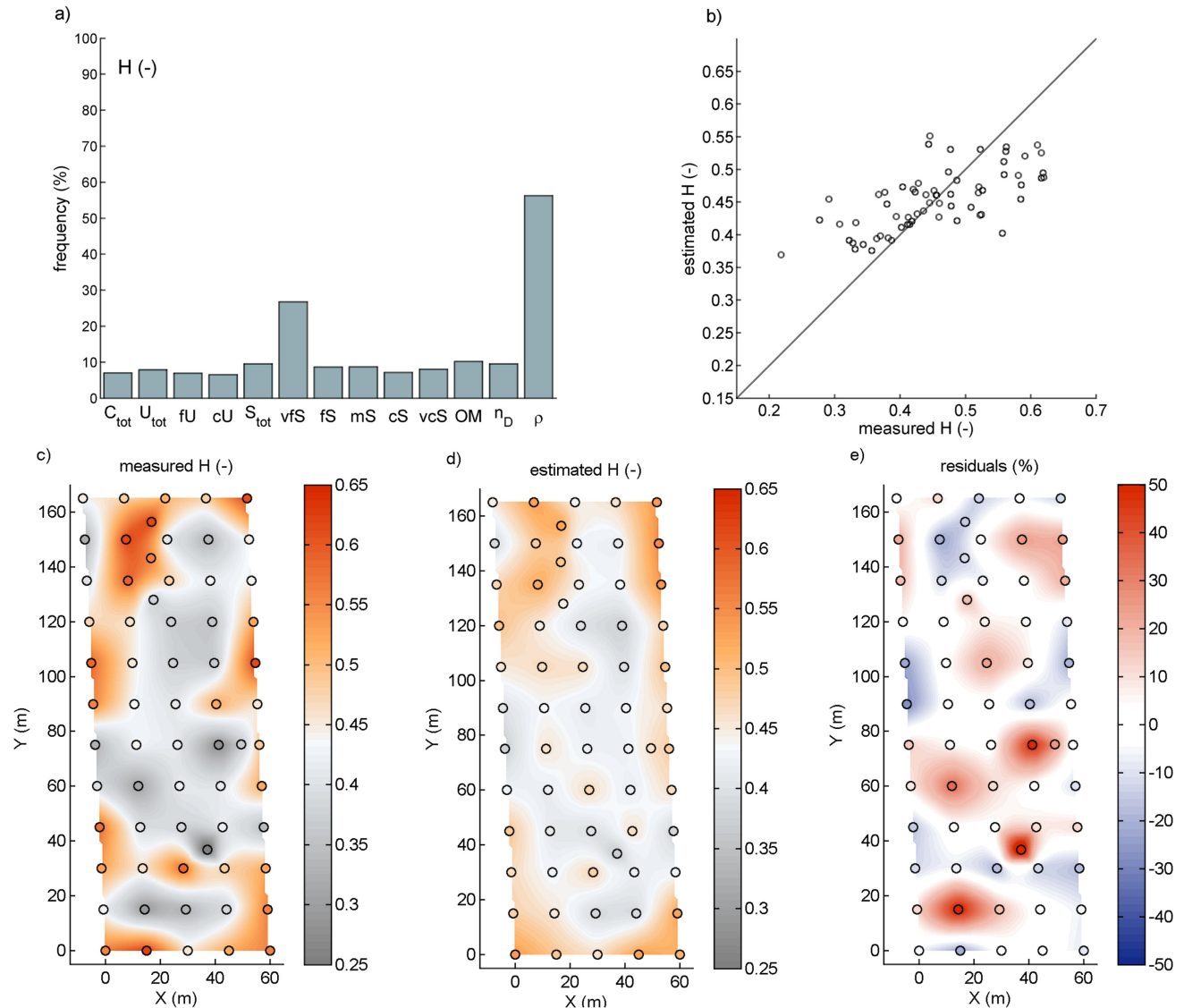


Figure 12. (a) The frequency at which the predictor variables were included into the best subset during the bootstrapping approach for the nongreedy subset selection for predicting the holdback H ; (b) the measured and estimated holdback H as estimated from the regression relationship shown in Table 5 ($R^2=0.41$); (c) the measured holdback H ; (d) the estimated holdback H using the regression relationship shown in Table 5; and (e) the residuals between the measured and estimated holdbacks using the formula $(H_{est}-H_{meas})/H_{meas} \times 100$.

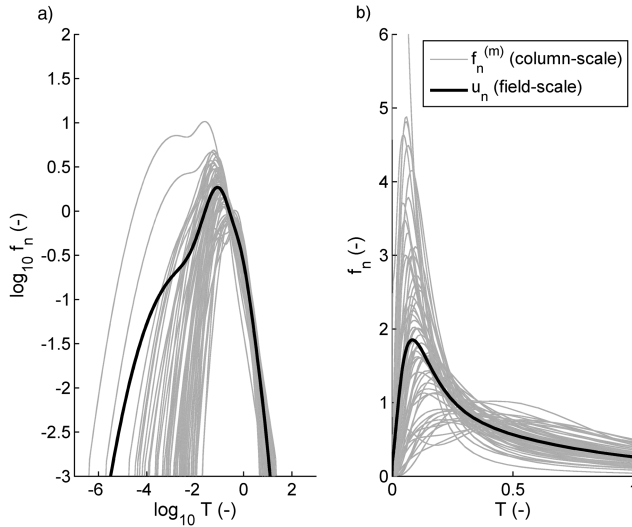


Figure 13. Column-scale and field-scale transport-time PDFs, $f_n^{(m)}$ and u_n , respectively. The PDFs shown in (a) and (b) are identical. Only the scales are different, i.e., double-logarithmic scale for Figure 13a and linear scale for Figure 13b.

generally underestimated, whereas the minimum values were overestimated.

3.5. Field-Scale BTC

[41] Figure 13 shows the normalized field-scale PDF $u_n(t)$ in comparison to the column-scale PDFs $f_n^{(m)}(t)$. The field-scale BTC shape measures are listed in Table 4. The field-scale transport velocity v is upscaled by the harmonic mean of the local-scale velocities (Table 4). The differences between the harmonic mean of the local-scale velocities and the field-scale velocity was probably caused by numerical errors. The piston-flow-to-transport-velocity ratio η was similar on both scales. The three related shape measures apparent dispersivity λ_{app} , relative 5%-arrival time $p_{0.05}$, and holdback H indicate that the strength of preferential transport was stronger at the field than at the column scale. Table 4 also shows that using the column-scale-derived regression functions (Table 5) for estimating the field-scale BTC shape measures from the mean soil properties leads to values that are comparable to the median of the column-scale shape measures, an exception being the transport velocities. The field-scale transport velocity would thus be overestimated, whereas the strength of preferential characteristics would be underestimated.

[42] The field-scale transport-time PDF derived here applies only to the topmost 20 cm of the soil at the Silstrup field site. It may be speculated how the field-scale PDF would appear at a greater soil depth, e.g., 100 cm. We consider two scenarios in the following. First, if the transport velocities in transport direction are uncorrelated, the lateral solute mixing would approximate the convection-dispersion regime [e.g., Roth and Hammel, 1996]. Then, the apparent dispersivity would remain constant, whereas the relative 5%-arrival time would increase and the holdback decrease with transport distance. If however the transport velocities in the transport direction were correlated, the

apparent dispersivity would increase [e.g., Flühler *et al.*, 1996]. Examples would be the triggering of additional preferential transport paths at soil horizon boundaries or vertical earthworm channels over the whole soil horizon. The 5% arrival time (and holdback) would then either increase (decrease) to a lesser extent than in the above discussed scenario or remain constant. A mix of both the above described scenarios appears to be likely in the majority of cases [Flühler *et al.*, 1996]. The field-scale solute BTC at 100 cm depth will then exhibit a similar velocity and piston-flow-to-transport-velocity ratio but a larger dispersivity and relative 5%-arrival time and a smaller holdback than at a depth of 20 cm.

4. Conclusions

[43] We investigated the tracer BTCs on the soil columns collected from the cultivated topsoil at the Silstrup field site under the near-saturated hydrologic conditions. Of the 65 investigated BTC experiments, 64 showed strong preferential transport features. The correlation between the strength of preferential transport and water saturation suggests that macropore transport was the dominant process. The observed variations in the preferential transport strength were also positively correlated with the bulk density. This may be explained as follows: larger bulk densities presumably led to a decrease in near-saturated hydraulic conductivities and as a consequence the activation of larger macropores. Correlations between the BTC shapes and the organic carbon content or between the ratio between clay and organic carbon content were only observed for the transport velocity and the piston-flow-to-transport-velocity ratio.

[44] Our study provides further evidence that it is possible to estimate soil solute transport properties from soil properties such as soil texture or bulk density. As a corollary, our results suggest that more detailed information on the soil texture than the three USDA texture fractions clay, silt, and sand may be useful in this context. We demonstrated that various BTC shape measures were relatively well predicted using linear regression approaches involving the bulk density and the very fine sand fraction, even though all BTCs exhibited strong preferential transport and the respective shape measures only showed relatively small variability.

[45] It must be noted however that the regression functions presented here for the BTC shape measures cannot be simply generalized to other field sites. This is strongly suggested by the metastudy of 733 BTC experiments of Koestel *et al.* [2012] who found an opposite correlation between bulk density and strength of preferential transport to the one found in this study. An upscaling approach for estimating the field-scale BTC for the topsoil from the column-scale BTCs suggests that the regression relationships between soil properties and column-scale BTCs yield wrong field-scale shape measures if applied to average field-scale soil properties. The transport velocity would be overestimated, and the strength of preferential transport underestimated.

[46] It is notable that we also found that the spatial correlation length of the investigated BTC shape measures was smaller than the sampling distance of 15 m. In the future,

studies aiming to establish predictive relationships for the soil solute transport properties should include data from noninvasive geophysical soil-mapping techniques like EM38 [Saey *et al.*, 2009] or γ -ray spectroscopy [van Egmond *et al.*, 2010] as a complement to traditionally measured soil properties. This would allow a better spatial resolution of the predictor variables and therefore also a better characterization of the variability of the soil solute transport properties. It would furthermore improve conditions for estimating solute transport properties at the field scale.

[47] **Acknowledgments.** This study was funded by the Danish Pesticide Leaching Assessment Program (www.pesticidvarsling.dk) and by the international project “Soil Infrastructure, Interfaces, and Translocation Processes in Inner Space (Soil-it-is)” which is funded by the Danish Research Council for Technology and Production Sciences (<http://www.agrsci.dk/soil-it-is/>).

References

- Addiscott, T. M., and N. J. Bailey (1990), Relating the parameters of a leaching model to the percentage of clay and other soil components, in *Field-Scale Water and Solute Flux in Soils*, edited by H. F. K. Roth, W. A. Jury, and J. C. Parker, pp. 209–221, Birkhauser Verl. AG, Basel, Switzerland.
- Bedmar, F., J. L. Costa, and D. Gimenez (2008), Column tracer studies in surface and subsurface horizons of two typical argiudolls, *Soil Sci.*, 173(4), 237–247.
- Bloem, E., F. A. N. Hogervorst, and G. H. de Rooij (2009), A field experiment with variable-suction multi-compartment samplers to measure the spatio-temporal distribution of solute leaching in an agricultural soil, *J. Contam. Hydrol.*, 105(3–4), 131–145.
- Bouma, J. (1989), Using soil survey data for quantitative land evaluation, *Adv. Soil Sci.*, 9, 177–213.
- Bouma, J., and L. W. Dekker (1978), Case-study on infiltration into dry clay soil: 1. Morphological observations, *Geoderma*, 20(1), 27–40.
- Boutchko, R., V. L. Rayz, N. T. Vandehey, J. P. O’Neil, T. F. Budinger, P. S. Nico, J. L. Druhan, D. A. Saloner, G. T. Gullberg, and W. W. Moses (2012), Imaging and modeling of flow in porous media using clinical nuclear emission tomography systems and computational fluid dynamics, *J. Appl. Geophys.*, 76, 74–81.
- Bronswijk, J. J. B., W. Hamminga, and K. Oostindie (1995), Field-scale solute transport in a heavy clay soil, *Water Resour. Res.*, 31(3), 517–526.
- Butters, G. L., W. A. Jury, and F. F. Ernst (1989), Field scale transport of bromide in an unsaturated soil: 1. Experimental methodology and results, *Water Resour. Res.*, 25(7), 1575–1581.
- Carminati, A., A. Kaestner, P. Lehmann, and H. Flühler (2008), Unsaturated water flow across soil aggregate contacts, *Adv. Water Resour.*, 31(9), 1221–1232.
- Christakos, G. (2000), *Modern Spatiotemporal Geostatistics*, 304 pp., Oxford Univ. Press, New York.
- Coats, K. H., and B. D. Smith (1964), Dead-end pore volume and dispersion in porous media, *Soc. Pet. Eng. J.*, 4(1), 73–84.
- Danckwerts, P. V. (1953), Continuous flow systems—Distribution of residence times, *Chem. Eng. Sci.*, 2(1), 1–13.
- de Jonge, L. W., P. Moldrup, G. H. Rubaek, K. Schelde, and J. Djurhuus (2004), Particle leaching and particle-facilitated transport of phosphorus at field scale, *Vadose Zone J.*, 3(2), 462–470.
- de Jonge, L. W., P. Moldrup, and P. Schjønning (2009), Soil infrastructure, interfaces and translocation processes in inner space (‘soil-it-is’): Towards a road map for the constraints and crossroads of soil architecture and biophysical processes, *Hydrol. Earth Syst. Sci.*, 13(8), 1485–1502.
- Dexter, A. R., G. Richard, D. Arrouays, E. A. Czyz, C. Jolivet, and O. Duval (2008), Complexed organic matter controls soil physical properties, *Geoderma*, 144(3–4), 620–627.
- Flühler, H., W. Durner, and M. Flury (1996), Lateral solute mixing processes—A key for understanding field-scale transport of water and solutes, *Geoderma*, 70(2–4), 165–183.
- Flury, M., H. Flühler, W. A. Jury, and J. Leuenberger (1994), Susceptibility of soils to preferential flow and water—A field study, *Water Resour. Res.*, 30(7), 1945–1954.
- Gee, G. W., and D. Or (2002), *Methods of Soil Analysis: Part 4. Physical Methods, Book Series*, vol. 5, Sci. Soc. of Am., Madison, Wis.
- Glueckauf, E., K. H. Barker, and G. P. Kitt (1949), Theory of chromatography: 8. The separation of lithium isotopes by ion exchange and of neon isotopes by low-temperature adsorption columns, *Discuss. Faraday Soc.*, 7, 199–213.
- Goncalves, M. C., F. J. Leij, and M. G. Schaap (2001), Pedotransfer functions for solute transport parameters of Portuguese soils, *Eur. J. Soil Sci.*, 52(4), 563–574.
- Hastie, T., R. Tibshirani, and J. H. Friedman (2009), *The Elements of Statistical Learning: Data Mining, Inference, and Prediction*, Springer, New York, N. Y.
- Horn, R., H. Taubner, M. Wuttke, and T. Baumgartl (1994), Soil physical properties related to soil structure, *Soil Tillage Res.*, 30(2–4), 187–216.
- Iversen, B. V., C. D. Børgesen, M. Lægdsmand, M. H. Greve, G. Heckrath, and C. Kjærgaard (2011), Risk predicting of macropore flow using pedotransfer functions, textural maps, and modeling, *Vadose Zone J.*, 10(4), 1185–1195.
- Jarvis, N. J. (2007), A review of nonequilibrium water flow and solute transport in soil macropores: Principles, controlling factors and consequences for water quality, *Eur. J. Soil Sci.*, 58(3), 523–546.
- Jarvis, N. J., J. Moeys, J. M. Hollis, S. Reichenberger, A. M. L. Lindahl, and I. G. Dubus (2009), A conceptual model of soil susceptibility to macropore flow, *Vadose Zone J.*, 8(4), 902–910.
- Jarvis, N. J., J. Moeys, J. K. Koestel, and J. M. Hollis (2012), Preferential flow in a pedological perspective, in *Hydropedology: Synergistic Integration of Soil Science and Hydrology*, edited by Henry Lin, Elsevier, Amsterdam.
- Jury, W. A., and K. Roth (1990), *Transfer Functions and Solute Movement Through Soil: Theory and Applications*, 226 pp., Birkhauser Verl. AG, Basel, Switzerland.
- Kasteel, R., M. Burkhardt, S. Giesa, and H. Vereecken (2005), Characterization of field tracer transport using high-resolution images, *Vadose Zone J.*, 4(1), 101–111.
- Kjær, J., P. Olsen, K. Bach, H. C. Barlebo, F. Ingerslev, M. Hansen, and B. H. Sorensen (2007), Leaching of estrogenic hormones from manure-treated structured soils, *Environ. Sci. Technol.*, 41, 3911–3917, doi:10.1021/es0627747.
- Knudby, C., and J. Carrera (2005), On the relationship between indicators of geostatistical, flow and transport connectivity, *Adv. Water Resour.*, 28(4), 405–421.
- Koestel, J., J. Vanderborght, M. Javaux, A. Kemna, A. Binley, and H. Vereecken (2009), Noninvasive 3-D transport characterization in a sandy soil using ERT: 2. Transport process inference, *Vadose Zone J.*, 8(3), 723–734.
- Koestel, J., J. Moeys, and N. J. Jarvis (2011), Evaluation of nonparametric shape measures for solute breakthrough curves, *Vadose Zone J.*, 10(4), 1261–1275.
- Koestel, J., J. Moeys, and N. Jarvis (2012), Meta-analysis of the effects of soil properties, site factors and experimental conditions on preferential solute transport, *Hydrol. Earth Syst. Sci.*, 16(6), 1647–1665.
- Kolenbrander, G. J. (1970), Calculation of parameters for evaluation of leaching of salts under field conditions, illustrated by nitrate, *Plant Soil*, 32(2), 439–453.
- Kurunc, A., S. Ersahin, B. Y. Uz, N. K. Sonmez, I. Uz, H. Kaman, G. E. Bacalan, and Y. Emekli (2011), Identification of nitrate leaching hot spots in a large area with contrasting soil texture and management, *Agric. Water Manage.*, 98(6), 1013–1019.
- Lennartz, B., S. K. Kamra, and S. Meyer-Windel (1997), Field scale variability of solute transport parameters and related soil properties, *Hydrol. Earth Syst. Sci.*, 1(4), 801–811.
- Lindhardt, B., C. Abildtrup, H. Vosgerau, P. Olsen, S. Torp, B. V. Iversen, J. O. Jørgensen, F. Plauborg, P. Rasmussen, and P. Gravesen (2001), *The Danish Pesticide Leaching Assessment Programme—Site Characterization and Monitoring Design*, Geol. Surv. of Den. and Greenl., Copenhagen, Denmark.
- Mallants, D., M. Vanclooster, and J. Feyen (1996), Transect study on solute transport in a macroporous soil, *Hydrol. Processes*, 10(1), 55–70.
- Nielsen, D. R., and J. W. Biggar (1962), Miscible displacement: III. Theoretical considerations, *Soil Sci. Soc. Am. Proc.*, 26(3), 216–221.
- Norgaard, T., P. Moldrup, P. Olsen, A. L. Vendelboe, B. V. Iversen, M. H. Greve, J. Kjær, and L. W. de Jonge (2012), Comparative mapping of soil physical-chemical and structural parameters at field scale to identify zones of enhanced leaching risk, *J. Environ. Qual.*, 42, 271–283, doi:10.2134/jeq2012.0105.

- Petersen, C. T., S. Hansen, and H. E. Jensen (1997), Tillage-induced horizontal periodicity of preferential flow in the root zone, *Soil Sci. Soc. Am. J.*, 61(2), 586–594.
- Poulsen, T. G., P. Moldrup, L. W. de Jonge, and T. Komatsu (2006), Colloid and bromide transport in undisturbed soil columns: Application of two-region model, *Vadose Zone J.*, 5(2), 649–656.
- Quisenberry, V. L., B. R. Smith, R. E. Phillips, H. D. Scott, and S. Nortcliff (1993), A soil classification-system for describing water and chemical transport, *Soil Sci.*, 156(5), 306–315.
- Rawls, W. J. (1983), Estimating soil bulk-density from particle-size analysis and organic-matter content, *Soil Sci.*, 135(2), 123–125.
- Rose, D. A. (1973), Some aspects of hydrodynamic dispersion of solutes in porous materials, *J. Soil Sci.*, 24(3), 285–295.
- Rose, D. A., F. Abbas, and M. A. Adey (2009), The effect of surface-solute interactions on the transport of solutes through porous materials, *Eur. J. Soil Sci.*, 60(3), 398–411.
- Roth, K., and K. Hammel (1996), Transport of conservative chemical through an unsaturated two-dimensional Miller-similar medium with steady state flow, *Water Resour. Res.*, 32(6), 1653–1663.
- Roulier, S., and N. Jarvis (2003), Modeling macropore flow effects on pesticide leaching: Inverse parameter estimation using microlysimeters, *J. Environ. Qual.*, 32(6), 2341–2353.
- Saey, T., M. van Meirvenne, H. Vermeersch, N. Ameloot, and L. Cockx (2009), A pedotransfer function to evaluate the soil profile textural heterogeneity using proximally sensed apparent electrical conductivity, *Geoderma*, 150(3–4), 389–395.
- Schaap, M. G., F. J. Leij, and M. T. van Genuchten (1998), Neural network analysis for hierarchical prediction of soil hydraulic properties, *Soil Sci. Soc. Am. J.*, 62(4), 847–855.
- Schlueter, S., U. Weller, and H.-J. Vogel (2011), Soil-structure development including seasonal dynamics in a long-term fertilization experiment, *J. Plant Nutr. Soil Sci.*, 174(3), 395–403.
- Schotanus, D., M. J. van der Ploeg, and S. E. A. T. M. van der Zee (2012), Quantifying heterogeneous transport of a tracer and a degradable contaminant in the field, with snowmelt and irrigation, *Hydrol. Earth Syst. Sci.*, 16(8), 2871–2882.
- Shaffer, M. J., B. K. Wylie, and M. D. Hall (1995), Identification and mitigation of nitrate leaching hot spots using NLEAP-GIS technology, *J. Contam. Hydrol.*, 20(3–4), 253–263.
- Shaw, J. N., L. T. West, D. E. Radcliffe, and D. D. Bosch (2000), Preferential flow and pedotransfer functions for transport properties in sandy Kandiudults, *Soil Sci. Soc. Am. J.*, 64(2), 670–678.
- Sibson, R. (1981), *A brief description of natural neighbor interpolation*, in *Interpreting Multivariate Data*, edited by V. Barnett, pp. 21–36, Wiley, Chichester, U. K.
- Smith, E. A., W. L. Powers, and P. J. Shea (1995), Relationship of bromide and atrazine movement in soil to pore/size distribution, compaction and saturation cycles, *Soil Sci.*, 159(1), 23–31.
- Thomas, G. W., and A. R. Swoboda (1970), Anion exclusion effects on chloride movement in soils, *Soil Sci.*, 110(3), 163–166.
- Tranter, G., B. Minasny, A. B. McBratney, B. Murphy, N. J. McKenzie, M. Grundy, and D. Brough (2007), Building and testing conceptual and empirical models for predicting soil bulk density, *Soil Use Manage.*, 23(4), 437–443.
- van Egmond, F. M., E. H. Loonstra, and J. Limburg (2010), *Gamma ray sensor for topsoil mapping: The Mole*, in *Proximal Soil Sensing*, edited by R. A. Viscarra Rossel, A. B. McBratney, and B. Minasny, pp. 323–332, Springer Netherlands, Dordrecht.
- van Genuchten, M. T., and P. J. Wierenga (1976), Mass-transfer studies in sorbing porous-media: 1. Analytical solutions, *Soil Sci. Soc. Am. J.*, 40(4), 473–480.
- Vanderborght, J., and H. Vereecken (2007), Review of dispersivities for transport modeling in soils, *Vadose Zone J.*, 6(1), 29–52.
- Vanderborght, J., et al. (2001), Overview of inert tracer experiments in key Belgian soil types: Relation between transport and soil morphological and hydraulic properties, *Water Resour. Res.*, 37(12), 2873–2888.
- Vereecken, H., J. Maes, J. Feyen, and P. Darius (1989), Estimating the soil-moisture retention characteristic from texture, bulk-density, and carbon content, *Soil Sci.*, 148(6), 389–403.
- Vereecken, H., M. Weynants, M. Javaux, Y. Pachepsky, M. G. Schaap, and M. T. v. Genuchten (2010), Using pedotransfer functions to estimate the van Genuchten–Mualem soil hydraulic properties: A review, *Vadose Zone J.*, 9(4), 795–820.
- Vervoort, R. W., D. E. Radcliffe, and L. T. West (1999), Soil structure development and preferential solute flow, *Water Resour. Res.*, 35(4), 913–928.
- Vogel, H. J. (2000), A numerical experiment on pore size, pore connectivity, water retention, permeability, and solute transport using network models, *Eur. J. Soil Sci.*, 51(1), 99–105.
- Vogel, H. J., and K. Roth (2003), Moving through scales of flow and transport in soil, *J. Hydrol.*, 272(1–4), 95–106.
- Wang, W., A. N. Kravchenko, A. J. M. Smucker, W. Liang, and M. L. Rivers (2012), Intra-aggregate pore characteristics: X-ray computed microtomography analysis, *Soil Sci. Soc. Am. J.*, 76(4), 1159–1171.
- Wild, A., and I. A. Babiker (1976), Asymmetric leaching pattern of nitrate and chloride in a loamy sand under field conditions, *J. Soil Sci.*, 27(4), 460–466.
- Wösten, J. H. M., Y. A. Pachepsky, and W. J. Rawls (2001), Pedotransfer functions: Bridging the gap between available basic soil data and missing soil hydraulic characteristics, *J. Hydrol.*, 251(3–4), 123–150.